Research paper

Modeling a class of thermal ice probes for accessing the solar system's ocean worlds

Michael J. Durka [a,b,*], Miles W.E. Smith [a], Michael J. Ullman [b,c], Bailey Cassler [a,b], Richard Otis [a], Thomas A. Cwik [a], Benjamin J. Hockman [a], Matthew M. Barry [b]

[a] *Jet Propulsion Laboratory, California Institute of Technology, 4800 Oak Grove Drive, Pasadena, CA 91109, United States of America*
[b] *University of Pittsburgh, Department of Mechanical Engineering and Materials Science, 3700 O'Hara Street, Pittsburgh, PA 15261, United States of America*
[c] *University of Michigan, Department of Aerospace Engineering, 1320 Beal Avenue, Ann Arbor, MI 48109, United States of America*

ARTICLE INFO

ABSTRACT

The subsurface oceans of icy moons in the outer solar system are prime candidates for harboring extra-terrestrial life. Missions to melt through the ice shells of these worlds utilizing an ice probe or "cryobot" to access the oceans have been proposed. To design such a cryobot for a successful mission, the relationship between a cryobot's heat budget and descent speed within any given environment must be understood. Large uncertainties in the ice shell thickness and temperature profile require that the problem be treated via probabilistic techniques, such as a Monte Carlo simulation. By contrast, the speed of a cryobot descending through ice with specified far-field temperature and material properties can, in principle, be quantified with little uncertainty. A model of cryobot performance that can be computed quickly and accurately will save significant computational time for the broader simulation, and allow for the mission's basic thermal needs to be understood. The work reported here builds upon an existing analytic thermal model of ice probes that, while suitable for terrestrial conditions, begins to incur potentially problematic errors in extraterrestrial environments. The new model provides improvement to the previous model for flight-relevant probes in extra-terrestrial ice conditions, predicting the total heat budget to within 1.2% of high-fidelity numerical simulations while requiring a small fraction of the computational time. The model can be non-dimensionalized in a compact form, making it suitable for modeling a broad class of cylindrical ice probes in a probabilistic modeling framework for determining the time required to access the sub-surface ocean. Such models can then provide the high-level requirements for cryobot system architectures that will enable successful ocean-access missions.

1. Introduction

The ocean worlds of Europa and Enceledus are among the most promising locations for life beyond Earth, and missions to access the subsurface oceans of these icy moons have been proposed [2–5]. Ocean access concepts center around an ice probe or "cryobot" that uses heat to descend through the ice shell. Ice is melted below the probe, with the resulting liquid flowing around the sides and refreezing above the probe[1] [6].

To melt through several kilometers of ice shell, the probe must carry a self-contained energy source, such as a Radioisotope Thermoelectric Generator (RTG) or a small fission reactor. The mass, heat density,

and electrical output of these systems drive the design of the ice probe and the overall mission architecture [7]. Namely, systems with higher energy density enable faster descent times and/or larger payloads to be carried to the ocean. A critical driving factor in determining the appropriate energy density for such a mission is the local ambient ice environment, which changes substantially with depth. For example, temperatures in the Europan ice shell are expected to range from approximately 100 K at the surface to the local melting temperature of ice at the ice–ocean interface [8]. As the probe descends, it must adapt to these changing conditions. In colder regions, more heat must be directed to the probe's side walls to prevent freezing of the melt

---

[1] Transient periods may include an initiation phase where the ice is sublimating in the vacuum environment near the surface, non-vertical descent to avoid obstacles, and operation of a cutter to penetrate through difficult layers. However, it is anticipated that the hole above the probe will close at a relatively shallow depth [1], and the subsequent operation will be dominated by melting, resulting in steady-state, vertical descent.

Nomenclature

System geometry

(r, z)	Cylindrical coordinate system
δ_r	Thickness of side melt channel
L	Probe length
R_i	Probe radius
R_o	Cavity radius
r^*	Ratio of probe radius to cavity radius

Material properties

α_L	Thermal diffusivity of water at melt point
α_s	Thermal diffusivity of ice at melt point
α	Temperature-dependent thermal diffusivity
c_L	Specific heat capacity of water at melt point
c_s	Specific heat capacity of ice at melt point
c	Temperature-dependent specific heat capacity
H	Heat of fusion of water
k_L	Thermal conductivity of water at melt point
k_s	Thermal conductivity of ice at melt point
k	Temperature-dependent thermal conductivity
ρ_L	Density of water at melt point
ρ_s	Density of ice at melt point
ρ	Temperature-dependent density of ice
λ	Ratio of material properties $c_s T_0 / H$
β	Ratio of material properties $c_L k_s / (c_s k_L)$

Ice probe thermal modeling

T	Temperature
T_0	Melt point temperature
T_∞	Far-field temperature
Θ	Non-dimensional far-field temperature
ϵ	Probe efficiency
Ω	Non-dimensional total heat per unit length
$\dot{q}''$	Heat flux
$\dot{Q}_{\text{ref}}$	Reference heat
$\dot{Q}_{\text{tot}}$	Total cryobot heat
$\dot{Q}_k$	Partition of cryobot heat lost through path k

Miscellaneous

D	Ice shell thickness
$\mathcal{J}_1$	Jaeger Integral of the first kind
$\mathcal{J}_0$	Jaeger Integral of the zeroth kind
τ	Non-dimensional probe response
t_d	Time to descend through ice shell
$\vec{v}$	Probe velocity
v	Unsigned probe speed
z_d	Distance from ice surface to probe tip

water surrounding the hull; whereas in warmer regions, the sidewall heat requirement is substantially less. Consequently, the remaining heat that can be directed forward to enable descent will vary with depth. Therefore, programmatic concerns of landed mass, payload volume, and the time to reach the ocean can only be assessed with the aid of an accurate thermal model that predicts probe performance in every local environment the probe will encounter.

However, these assessments remain challenging due to the large present uncertainties in thickness of the Europan ice shell, with estimates of 12–36 km for the likely range [8]. These uncertainties in thickness propagate into uncertainties in far-field temperature as a function of depth. As a result, probabilistic modeling is presently the most viable means of estimating the time-to-ocean for a given probe design. Enabling such an analysis to be conducted in a reasonable timeframe would rely on fast-computing models relating a given cryobot's total thermal budget $\dot{Q}_{\text{tot}}$ to the instantaneous probe descent speed v at any given far-field temperature T_∞. Such models can advantageously leverage the computational simplicity of compact, non-dimensionalized analytic solutions as much as possible.

One such model for long cylindrical ice probes originates from the work of Aamot [9]. Among many other assumptions, the Aamot model assumes temperature-independent material properties and ignores the heat advected from the system by the melt water. The model is fully-analytic, and therefore its solution can be computed rapidly. Dating as far back as the original author, experimental results have demonstrated approximate agreement with the model under a limited range of conditions. However, more recent results, especially from testing in cryogenic ice to simulate conditions on Europa, have demonstrated significant discrepancies [1,10]. In one example given in [1], the heat required to achieve a given speed was found to be 50% above the model prediction. Without both understanding and correcting these errors, serious programmatic concerns could be raised towards a Europan ocean-access mission.

To address such concerns, it was desirable to develop a modified version of the Aamot model based on the understanding and closing of these errors for foreseeable flight-relevant conditions. Additional confidence in the new model is gained by verifying its accuracy: comparing to benchmark cases derived from a high-fidelity numerical model in which most of the restrictive assumptions of the analytic model are removed. In particular, the modified Aamot model adds two relevant pieces of physics: (1) the temperature-dependence of ice material properties and (2) the water annulus surrounding the cryobot. In recognition of the pioneering work of the original author, and to convey the two-fold modification, we name the new model the *Aamot++ model*.

2. Modeling ice probe speed

Fig. 1 illustrates the basic elements of an axisymmetric system, with cylindrical coordinates r and z. An ice probe of length L is descending with speed v in the $-\hat{z}$ direction with the internal heat $\dot{Q}_{\text{tot}}$ distributed along its surface in a way that facilitates steady-state descent. A thin film of water develops below and around the circumference of the probe, opening up to a pool of melt water trailing behind the system. As discussed in [11], the internal heat must be distributed in a way that prevents the probe from becoming stalled by viscous forces acting along its side walls. Proper heat distribution results in the probe resting on a thin film of water at the front; the thickness of which can be neglected for the purpose of developing an analytic thermal model. As such, there is no distinction made between the probe length and the distance between the melt front and the entrance of the trailing melt pool. Operating in this regime, modulating the heat supplied to the front of the probe linearly modulates the descent rate. Conversely, heating along the side wall of the probe can result in a non-negligible side gap δ_r. Therefore, the distinction is made between an inner radius R_i, corresponding to the radius of the probe, and an outer radius R_o, corresponding to the radius of the cavity.

The system is studied in the co-moving reference frame of the probe. In this frame, a cylindrical boundary is defined such that it encompasses both the probe and the surrounding liquid film and truncates at the entrance to the trailing melt pool. The heat leaves the system via four possible paths. As the probe descends, new ice must be melted below it, absorbing an amount of heat $\dot{Q}_0$ to complete the phase change. In
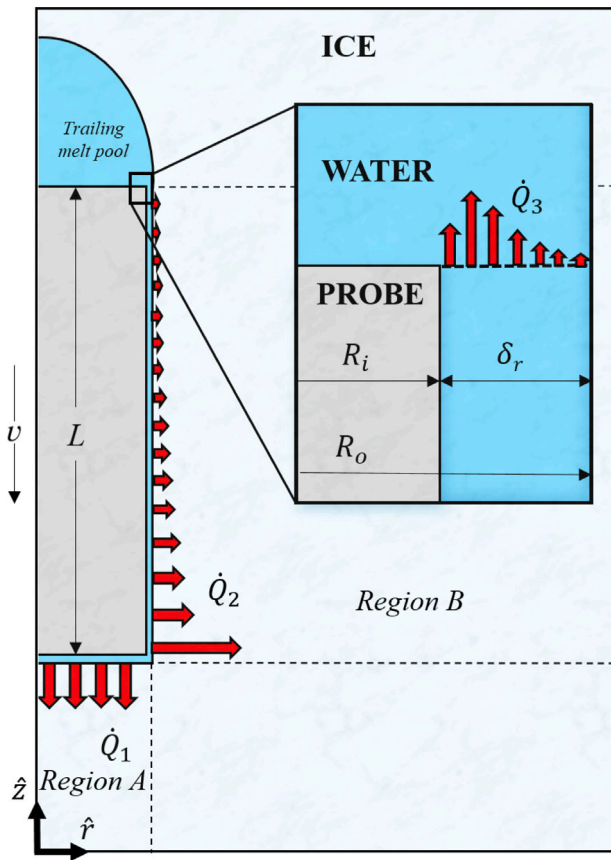
Fig. 1. The descending ice probe model schematic, showing the sensible heats leaving the domain.

order to warm the ice below the probe from the far-field temperature T_∞ to the melt-point temperature T_0, an additional amount of heat $\dot{Q}_1$ is conducted in the $-\hat{z}$ direction into the ice directly below the probe. Heat is also diffused radially along the cylindrical bounding surface at R_o where the temperature is also T_0. The heat flux $\dot{q}_2''$ along this surface is large for low values of z, where the probe encounters unperturbed ambient ice and the temperature gradients are steepest. However, the flux falls off rapidly with increasing z, where the surrounding ice has been warmed by the passage of the probe. The integral of the flux along this bounding surface defines $\dot{Q}_2$. Finally, melt water flowing across the rear boundary into the trailing melt pool will carry heat by advection, including the energy stored by the phase change. If this water is warmed above T_0, additional heat unused in melting or warming the surrounding ice will be carried out of the system. The term $\dot{Q}_3$ representing this heat loss by advection completes the heat budget assuming an efficient design in that the rear-facing hull is thermally insulated (at $z = L$). The total heat is given by summing all of the terms

$$\dot{Q}_{\text{tot}} = \dot{Q}_0 + \dot{Q}_1 + \dot{Q}_2 + \dot{Q}_3 \tag{1}$$

Under an assumption of steady-state behavior, no other paths exist for heat to exit the system. In [12], the authors consider heat advecting from the thin film at the front of the probe into the side annulus which is an *internal* transfer of heat. Some of this heat will offset the heat that must be supplied by the probe sidewall to balance $\dot{Q}_2$. For probes significantly shorter than 1 m, the authors show that some of this heat will survive to the rear of the system and contribute to $\dot{Q}_3$. However, for realistic flight designs that are expected to be significantly longer, this heat will not contribute to the $\dot{Q}_3$ term in practice.

The term $\dot{Q}_0$ is easily determined as the product of the specific latent heat of fusion H and the mass flux through the lower boundary. As

described in [11], the term $\dot{Q}_3$ is accessible by studying the radial heat transport across the thin film δ_r which leads to a warming of the fluid as it flows through the melt channel. The terms $\dot{Q}_1$ and $\dot{Q}_2$ must be determined by studying the transport of heat through the ice. Under the assumptions of steady-state descent and cylindrical symmetry, the conduction of heat in the ice region is governed by the diffusion–advection equation in the co-moving reference frame of the probe, given by

$$\frac{\partial}{\partial z}\left(-k\frac{\partial T}{\partial z}\right) + \frac{1}{r}\frac{\partial}{\partial r}\left(-kr\frac{\partial T}{\partial r}\right) + c\rho v\frac{\partial T}{\partial z} = 0 \tag{2}$$

where $T(r, z)$ is the temperature field in cylindrical coordinates, v is the unsigned speed of the probe, and k, c, and ρ are the thermal conductivity, specific heat capacity, and density of the ice respectively. In general, these properties are strongly temperature-dependent and weakly pressure-dependent. As such, only temperature dependence is accounted for in this paper, and any anisotropy in k is neglected. From left to right, the three terms of Eq. (2) are identified as (a) *axial diffusion*, (b) *radial diffusion*, and (c) *ice advection*, where the latter describes the upwards movement of ice in this reference frame.

The right hand side of Eq. (1) is understood to be a function of probe speed v, while the total available heat is typically a fixed design parameter. A terrestrial system will be limited by the amount of power that can be supplied via a tether, while an extraterrestrial probe will be limited by the fixed inventory of heat supplied from radioactive decay. As such, Eq. (1) must be inverted to determine the probe speed as a function of heat and other system parameters.

2.1. The Aamot solution

In 1967, H. W. C. Aamot proposed a solution to Eq. (2) for the case of temperature-*independent* material properties [9]. The solution was achieved by approximating the behavior in two separate regions of the ice domain — the column of material directly below the probe (Region A in Fig. 1) and the annular region surrounding the probe (Region B). A brief summary of the derivation is given here with additional details provided in Appendix A.

In the formulation given by Aamot, the annulus of melt water around the probe was not considered, so the radius of the system is taken to be the probe radius R_i. As such, the probe must melt ice at a rate $\dot{m} = \pi R_i^2 v \rho_s$, supplying latent heat H per unit mass to give

$$\dot{Q}_0 = \pi R_i^2 v \rho_s H \tag{3}$$

In Region A, the temperature contours are compressed by the relative motion of the ice such that the melt front can be treated as a portion of an infinite plate at temperature T_0. This enables the radial diffusion term in Eq. (2) to be neglected. Under this approximation, the heat required to warm the ice in Region A is given by

$$\dot{Q}_1 = \pi R_i^2 v \rho_s c_s \left(T_0 - T_\infty\right) \tag{4}$$

where the solid phase material properties have been replaced by their values at the melt point (k_s, ρ_s, c_s) and T_∞ is the far-field temperature. Note that the combination of Eqs. (3) and (4) is Eq. (4) in [9]. A careful explanation of the $\dot{Q}_0$ and $\dot{Q}_1$ terms is also given in [12], utilizing the Stefan model for a moving phase-change boundary.

In Region B, the dominating terms in Eq. (2) are the radial diffusion and ice advection terms. The axial diffusion term is only relevant near the end regions which are neglected under the assumption that $L \gg R$. The resulting equation can be solved exactly in terms of Bessel functions to give the temperature field in the ice [13]. The temperature gradient at $r = R_i$ can then be calculated to determine the heat flux

$$\dot{q}_2''(z) = \frac{k_s\left(T_0 - T_\infty\right)}{R_i}\frac{4}{\pi^2}\mathcal{J}_0\left(\frac{\alpha_s z}{R_i^2 v}\right) \tag{5}$$

appearing as Eq. (9) in [9]. Here, we have introduced the Jaeger Integral of the zeroth kind

$$\mathcal{J}_0(\xi) = \int_0^\infty \frac{db}{b} \frac{e^{-\xi b^2}}{J_0^2(b) + Y_0^2(b)} \quad (6)$$

where J_0 and Y_0 are Bessel functions of the first and second kind respectfully. Integrating over the cylindrical surface of the probe yields

$$\dot{Q}_2 = 2\pi R_i \int_0^L \dot{q}_2'' \, dz$$
$$= \pi R_i^2 v \rho_s c_s \left(T_0 - T_\infty\right) \frac{8}{\pi^2} \mathcal{J}_1(\tau) \quad (7)$$

Here, we have introduced the Jaeger Integral of the first kind

$$\mathcal{J}_1(\tau) = \int_0^\infty \frac{db}{b^3} \frac{1 - e^{-\tau b^2}}{J_0^2(b) + Y_0^2(b)} \quad (8)$$

where the non-dimensional variable τ to be inversely proportional to the probe speed and is defined as

$$\tau = \frac{\alpha_s L}{v R_i^2} \quad (9)$$

The material properties of the solid phase are collected into the thermal diffusivity α_s evaluated at the melt point since the material properties are all assumed to be temperature-independent for this model.

Finally, Aamot does not consider the advective heat loss associated with liquid water flowing out of the back of the system, resulting in $\dot{Q}_3 = 0$. Combining the results as $\dot{Q}_{tot} = \dot{Q}_0 + \dot{Q}_1 + \dot{Q}_2 + \dot{Q}_3$ leads to the total heat as a function of the probe dimensions and speed, as well as the ice material properties and far-field temperature. By further defining non-dimensional quantities

$$\Theta = \frac{T_0 - T_\infty}{T_0}$$
$$\lambda = \frac{c_s T_0}{H}$$
$$\Omega = \frac{\dot{Q}_{tot}}{\dot{Q}_{ref}} \quad (10)$$

where $\dot{Q}_{ref} = \pi H \rho_s \alpha_s L$, the solution collapses to a compact non-dimensional form

$$\Omega \tau = 1 + \lambda \Theta \left\{ 1 + \frac{8}{\pi^2} \mathcal{J}_1(\tau) \right\} \quad (11)$$

Eq. (11) represents an extraordinary simplification. Under the assumptions of Aamot, the performance of any long, cylindrical ice probe operating under any far-field conditions collapses to a two-dimensional function $\tau(\Omega, \lambda\Theta)$.

The speed of the probe is determined by solving Eq. (11) for τ as a function of the design variable Ω and the environmental conditions as summarized by $\lambda\Theta$. An exact solution is obtainable upon specifying the boundary conditions $T = T_0$ on R_i, $T = T_\infty$ at $r = \infty$ and $z = -\infty$.

Dependence on other variables, such as probe dimensions or specific material properties, is given by analytically redimensionalizing.

2.2. The Aamot++ solution

The result of Section 2.1 provides relatively good agreement with numerical models and empirical measurements for warm ice that might be found in terrestrial glaciers [9]. However, for colder ice, the model begins to show disagreements of up to 50% with empirical data [1,10]. Additional disagreements can be produced by widening the water annulus to increase the advective heat loss $\dot{Q}_3$. These issues will arise for any realistic ice probe accessing the subsurface oceans of Europa or Enceladus. To enable the study of realistic mission concepts, the Aamot model is modified by: (1) Treating the material properties as temperature-*dependent* and (2) Adding a narrow annulus of water around the probe that both contributes to the net radius and advects

heat out the back of the system. The details of these changes are given in Appendix A while a brief summary is given here. In recognition of the pioneering work of the original author, we name this modified model Aamot++.

The $\dot{Q}_0$ term is modified only because the radius of the ice column being melted increases from R_i to R_o in order to generate the annular gap.

$$\dot{Q}_0 = \pi R_o^2 v \rho_s H \quad (12)$$

The $\dot{Q}_1$ term also increases because of the increased radius but is additionally modified by the temperature dependence of the material properties as explained in A.3. Temperature dependence on the material properties must now be introduced, and in this work are taken from [14].

$$\dot{Q}_1 = \pi R_o^2 v c_s \rho_s \left(T_0 - T_\infty\right) f_1$$
$$f_1 = \frac{\int_{T_\infty}^{T_0} \rho c \, dT}{c_s \rho_s \left(T_0 - T_\infty\right)} \quad (13)$$

If the material properties are independent of temperature then $f_1 = 1$, restoring the Aamot equation (4).

The calculation of $\dot{Q}_2$ is more involved. For temperature-dependent material properties, the governing equation in Region B is given by

$$\frac{1}{r} \frac{\partial}{\partial r} \left(-k r \frac{\partial T}{\partial r}\right) + c\rho v \frac{\partial T}{\partial z} = 0 \quad (14)$$

which is the one-dimensional (1D) radial, nonlinear diffusion equation with z/v serving as the time variable in the moving reference frame. The boundary condition $T = T_0$ is now located at the cylinder $r = R_o$. The temperature field $T(r, z)$ can in principle be solved for and differentiated at the boundary to give the radial flux. The radial flux can then be integrated over the boundary to obtain the heat $\dot{Q}_2$.

In practice, the nonlinearity of Eq. (14) means that an exact solution cannot be found. However, much can be learned from a careful dimensional analysis, indicating that the form of the solution must be

$$\dot{Q}_2 = \pi R_o^2 v \rho_s c_s \left(T_0 - T_\infty\right) f_2 \left(r^{*2}\tau, \Theta\right) \quad (15)$$

where R_o replaces R_i, and f_2 replaces the function $8\mathcal{J}_1(\tau)/\pi^2$ that appears for the Aamot solution. The variable τ has also been re-scaled because the boundary condition has moved, leading to the definition of the ratio

$$r^* = \frac{R_i}{R_o} \quad (16)$$

Additionally, f_2 now depends on the non-dimensional far-field temperature $\Theta = (T_0 - T_\infty)/T_0$, whereas for the Aamot solution, $8\mathcal{J}_1(\tau)/\pi^2$ was temperature-independent. However, there are no further degrees of freedom. If the shape of the function $\alpha(T)/\alpha_s$ is provided, f_2 can only depend on the terms $r^{*2}\tau$ and Θ.

In general, Eq. (14) must be solved numerically. The resulting function f_2 will depend on how the material properties depend on temperature, which could be significantly affected by impurities or the structure of the ice. Considered here is the case of pure ice of type 1 h, typical of terrestrial ice at atmospheric pressure[2] and described by the material properties given in [15,16]. For this case, numerical solutions to Eq. (14) were found for far-field temperatures ranging from 100 K to 270 K and for $r^{*2}\tau$ from 0.1 and 10 as described in A.5. Over this range, a compact analytic approximation to the function f_2 was identified.

$$\frac{f_2 \left(r^{*2}\tau, \Theta\right)}{\frac{8}{\pi^2} \mathcal{J}_1 \left(r^{*2}\tau\right)} \approx 1 + \left[a_1\Theta + a_2\Theta^2\right] \left[1 + a_3 \ln\left(r^{*2}\tau\right) + a_4 \ln^2\left(r^{*2}\tau\right)\right] \quad (17)$$

---

[2] This choice is expected to provide an approximate worst-case predictor for probe performance. The material properties depend most strongly on temperature. After temperature, the next strongest dependence is on the ice salinity which tends to lower the thermal conductivity and *increase* probe speed.

a_1	a_2	a_3	a_4	a_5
0.07923	0.07180	0.51498	0.03730	0.24021

The polynomial coefficients $a_1 - a_4$ given in Table 1 were determined by fitting to the numerical results.

The previous Aamot solution corresponded to a different set of material properties that were independent of temperature. This leads to a different solution of Eq. (14) with the values for the coefficients given trivially by $a_1 = a_2 = a_3 = a_4 = 0$. Additionally, if there is no water gap, $r^* = 1$. Together, these limiting conditions restore the Aamot equation (7).

The Aamot++ model also includes a nonzero value for the advective heat loss $\dot{Q}_3$. The calculation of this term is discussed in [11], drawing on the work of [17]. A nonzero gap size is generated by a temperature gradient across the water annulus to prevent the probe from being frozen in. The heat needed to sustain a nonzero gap size leads to the advective loss. Several equivalent formulations for the advective heat loss are given in [11] based on alternate auxiliary quantities. The most convenient form is selected for model validation, given by

$$\dot{Q}_3 = \left(1 - a_5 \frac{\delta_r}{R_o}\right) \frac{\delta_r}{2\alpha_L} \frac{\rho_s}{\rho_L} \pi R_o^2 \upsilon \left. \dot{q}_2'' \right|_{z=L} \tag{18}$$

where $\delta_r = R_o - R_i$, and the coefficient $a_5 = 0.24021$ provides a second-order correction for the cylindrical geometry. The thermal diffusivity of the liquid phase α_L is assumed to be constant over the narrow temperature range of the melt water.

Utilizing Eq. (15), Eq. (18) can be rewritten as

$$\dot{Q}_3 = \pi R_o^2 \upsilon \rho_s c_s \left(T_0 - T_\infty\right) f_3\left(\tau, r^*, \Theta\right)$$
$$f_3\left(\tau, r^*, \Theta\right) = \frac{1}{4} \beta \left\{(1 - r^*) + a_5(1 - r^*)^2\right\} \partial_{(r^{*2}\tau)} f_2(r^{*2}\tau, \Theta)$$
$$\beta = \frac{c_L k_s}{c_s k_L} \tag{19}$$

The appearance of the derivative with respect to $r^{*2}\tau$ introduces the radial flux term evaluated at the back of the probe, as seen in Eq. (18). The material properties of the liquid phase, c_L and k_L, are evaluated at the melt point with values taken from [14].

The combined result $\dot{Q}_{tot} = \dot{Q}_0 + \dot{Q}_1 + \dot{Q}_2 + \dot{Q}_3$ can be written in a non-dimensional form by dividing Eqs. (12), (13), (15), and (19) by the reference value $\dot{Q}_{ref}$ to give

$$\Omega r^{*2} \tau = 1 + \lambda \Theta \left\{f_1 + f_2 + f_3\right\} \tag{20}$$

The Aamot++ model now predicts the performance of the probe by finding the solution $\tau(\Omega, \Theta, r^*)$ of Eq. (20), where Ω is a probe design parameter proportional to the total heat per unit length, and Θ describes the far-field environment. As τ appears on both sides of Eq. (20), it must be found iteratively as a function of the $\dot{Q}_{tot}$ which it explicitly produces. As before, the dependence on physical variables, such as probe speed υ, total heat $\dot{Q}_{tot}$, and probe dimensions R_i and L, is given by analytically redimensionalizing the solution. The original Aamot solution is recovered in the limit that material properties are independent of temperature and $R_o \to R_i$, leading to $f_1 \to 1$, $f_2 \to 8\mathcal{J}_1(\tau)/\pi^2$, and $f_3 \to 0$. In this case, the right hand side of Eq. (20) depends only on τ. The addition of temperature-dependent material properties to the model introduces Θ to the right hand side, and the addition of the water annulus introduces r^*.

2.3. Efficiency and the intermediate Aamot+ model

An additional non-dimensional variable r^* has been introduced above the set required to describe the Aamot++ model. While geometrically r^* is understood as the ratio of the probe radius to the cavity radius, it can also be understood as introducing an operational inefficiency. There are several useful ways to define efficiency ϵ. Here (different from [12]) efficiency is defined as the ratio of the minimum total heat required to operate (corresponding to $r^* = 1$) relative to the total heat of a degraded system (where $r^* < 1$).

$$\epsilon = \frac{\dot{Q}_{tot}(r^* = 1)}{\dot{Q}_{tot}(r^* < 1)}$$
$$= r^{*2} \frac{1 + \lambda \Theta \left\{f_1 + f_2 + f_3\right\}\big|_{r^*=1}}{1 + \lambda \Theta \left\{f_1 + f_2 + f_3\right\}\big|_{r^*<1}} \tag{21}$$

The numerator $\dot{Q}_{tot}(r^* = 1)$ defines an intermediate model, where the nonlinear diffusion has been taken into account but the further degradation due to the liquid annulus has not. This intermediate model is named Aamot+ to distinguish it from Aamot or Aamot++.

The function $\epsilon(\tau, \Theta, r^*)$ is monotonic in r^*, relating the efficiency of the system to the geometry of the water annulus. Here a specific model is provided for this relationship based on a criterion that the probe is maintaining a uniform side gap. In principle, however, the shape of the side gap will depend on the internal distribution of heat within the probe, leading to alternate versions of the function ϵ. While the internal thermal design of the probe is beyond the scope of this paper, a general formula can be written as

$$\dot{Q}_{tot} = \frac{\dot{Q}_{tot}(\text{Aamot+})}{\epsilon} \tag{22}$$

In the general case, ϵ must be determined by a specific boundary condition at the probe surface (as done in this paper) or a numerical model of the interior heat distribution. The simplest alternative would be a system that is designed to maintain ϵ as a constant, though whether such a result can be achieved by engineering design has not been assessed.

The key differences between the Aamot, Aamot+ and Aamot++ models are summarized in Table 2. In Section 3, the differences between the models are computed and compared to a numerical model of the system that incorporates a more complete description of the physics.

3. Model comparison and validation

In order to evaluate the impact of the restrictive set of assumptions that typically accompany analytic models, the models of Section 2 are compared to a high-fidelity numerical model where most of the restrictive assumptions have been removed. The numerical simulation was run for 12 benchmark cases, corresponding to a matrix of four probe descent speeds and three far-field temperatures. The temperature of the Europan ice shell varies from around 100 K at the surface to around 270 K near the ice–ocean interface [8]. As such, far-field temperatures of 110 K, 180 K, and 230 K were selected, corresponding to three representative conditions that the ice probe will meet. The results comparing the analytic model and numerical model are shown in Fig. 2.[3]

The numerical model, discussed in detail in Appendix B, is governed by the full continuity, Navier–Stokes, and energy equations containing both ice and water with temperature-dependent material properties.

---

[3] It is worth commenting that in most (if not all) physical situations, the probe heat would be the independent variable and the probe speed the dependent variable. However, in the context of the numerical methodology in Appendix B and the theoretical nature of this work, it makes most sense to reverse these plot axes here from the norm.
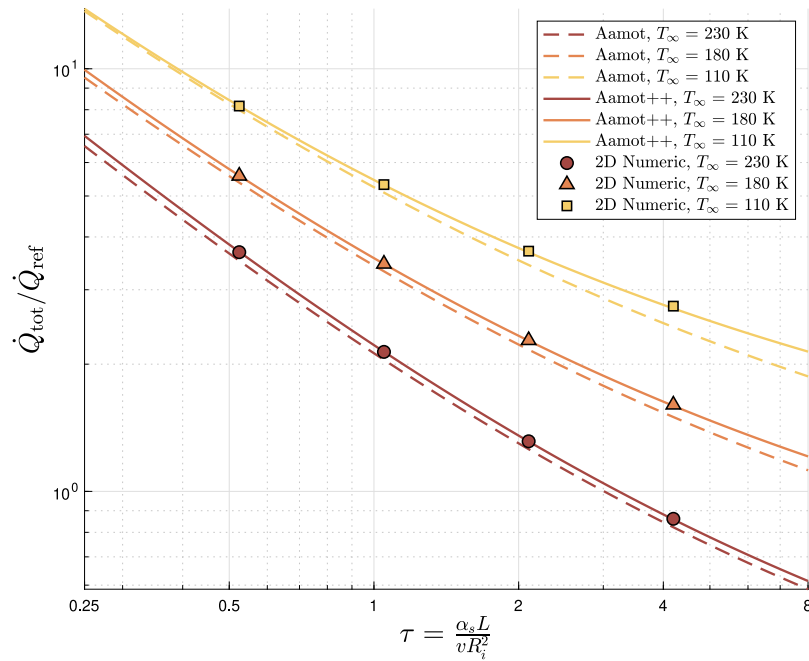
Fig. 2. Comparison of the Aamot and Aamot++ models to a numerical model with many fewer approximations, in which most notably, all terms in Eq. (2) are included throughout the domain. See Appendix B.2 for further details..

Table 2
Equations for determining probe speed as a function of heat per unit length and far-field temperature.

Decomposition of total heat		
$\dot{Q}_{tot} = \dot{Q}_0 + \dot{Q}_1 + \dot{Q}_2 + \dot{Q}_3$		
Latent heat (Eq. (12))	$\dot{Q}_0 = \frac{Q_{ref}}{r^{*2}\tau}$, $\dot{Q}_{ref} = \pi H \rho_s \alpha_s L$	
Axial diffusion (Eq. (13))	$\dot{Q}_1 = \frac{Q_{ref}}{r^{*2}\tau} \lambda\Theta f_1(\Theta)$	
Radial diffusion (Eq. (15))	$\dot{Q}_2 = \frac{Q_{ref}}{r^{*2}\tau} \lambda\Theta f_2(r^{*2}\tau,\Theta)$	
Advective loss (Eq. (18))	$\dot{Q}_3 = \frac{Q_{ref}}{r^{*2}\tau} \lambda\Theta f_3(\tau,r^*,\Theta)$	

Non-dimensional variables		
Far-field	$\Theta = \frac{T_0-T_\infty}{T_0}$	Materials	$\lambda = \frac{c_s T_0}{c_s \rho_s}$ $\beta = \frac{c_L k_s}{c_s k_L}$
Probe heat	$\Omega = \dot{Q}_{tot}/\dot{Q}_{ref}$	Probe speed	$\tau = \frac{\alpha_s L}{vR_i^2}$

Jaeger integrals

$\mathcal{J}_1(\tau) = \int_0^\infty \frac{db}{b^3} \frac{1-e^{-\tau b^2}}{J_0^2(b)+Y_0^2(b)}$ $\mathcal{J}_0(\tau) = \frac{d\mathcal{J}_1}{d\tau} = \int_0^\infty \frac{db}{b} \frac{e^{-\tau b^2}}{J_0^2(b)+Y_0^2(b)}$

See [18] for numerical method to calculate $\mathcal{J}_0$ and $\mathcal{J}_1$.

Functions for decomposing heat

$f_1(\Theta) = \int_0^\Theta \frac{c(\Theta')\rho(\Theta')}{c_s\rho_s} \frac{d\Theta'}{\Theta}$ where $\Theta' = \frac{T_0-T}{T_0}$ ($f_1 = 1$ for Aamot)
$f_2(r^{*2}\tau,\Theta) = \frac{8}{\pi^2}\mathcal{J}_1(r^{*2}\tau)\{1 + [a_1\Theta + a_2\Theta^2][1 + a_3\ln(r^{*2}\tau) + a_4\ln^2(r^{*2}\tau)]\}$
$f_3(\tau,r^*,\Theta) = \frac{1}{4}\beta\{(1-r^*) + a_5(1-r^*)^2\}\partial_{(r^{*2}\tau)}f_2(r^{*2}\tau,\Theta)$

Application to specific models			
	Aamot	Aamot+	Aamot++
	(Heritage model)	(+ Nonlinear diffusion)	(+ Liquid annulus, NL diff.)
c,ρ	c_s,ρ_s	Temperature dependent: $c(T)$, $\rho(T)$	
$a_1 - a_4$	0	Ice 1h: $\{0.07923, 0.07180, 0.51498, 0.03730\}$	
r^*, a_5	1, N/A	1, N/A	R_i/R_o, 0.24021

Non-dimensional total heat equation		
$\Omega r^{*2}\tau = 1 + \lambda\Theta(f_1+f_2+f_3)$		

The two-dimensional (2D) model retains the assumption of axial symmetry, but does not neglect the radial or axial diffusion terms in the forward and side annular regions respectively. The numerical model allows any desired water annulus shape to be considered, provided it is axisymmetric. The boundary conditions in the numerical cases were tailored to produce a vertical annulus such that R_o is constant, satisfying a required Aamot++ assumption. In all numerical cases compared with Aamot++, $r^* = 0.976$ at $z = L$. The simulations were completed with

dimensionful probe and environmental parameters and post-processed into the non-dimensional variables τ and Ω for comparison to the analytic results.

Fig. 3 shows the residual differences in the total heat budget between the advanced models and Aamot. For this particular comparison, two different versions of the numerical model are considered, designed to highlight the impact of relaxing Aamot-inherent assumptions. First, a numerical model is considered, having constant material properties and zero water jacket thickness, thus relaxing the assumption which neglects radial and axial diffusion in Regions A and B respectively (see Fig. 1). Even with these assumptions lifted, the Aamot model is seen to have excellent agreement with the linear, annulus-free numerical model. Next, when the non-constant material properties and water annulus is added to the numerical model, the Aamot model is seen to consistently under-predict the total heat budget computed by the numerical models. The most notable differences are for probes in cold ice that are either squat ($L/R \to 1$) or slow moving (as indicated by a higher value of τ). The Aamot++ model, however, closes with the numerical model to within 1.3%. Fig. 4 shows the successive addition of nonlinear diffusion only (Aamot+) and both nonlinear diffusion and a water annulus (Aamot++) to the original Aamot model. It is apparent that both modifications to the physics are necessary to achieve percent-level agreement with the numerical model and, indeed, the two modification combined are sufficient. Of the two modifications, the nonlinear diffusion is due to an unavoidable change in the behavior of the environment. On the other hand, the shape of the water annulus (and hence the efficiency) depends on the design of the heat distribution within the probe itself, illustrated here by a specific example. An idealized probe approaches the behavior of Aamot+ in the case that $\epsilon \to 1$.

4. Discussion

4.1. Application of the analytic models

The analytic models described in Sections 2.1, 2.2, and 2.3 can be applied to the calculation of the time t_d it will take to descend through a segment of an ice shell of thickness D.
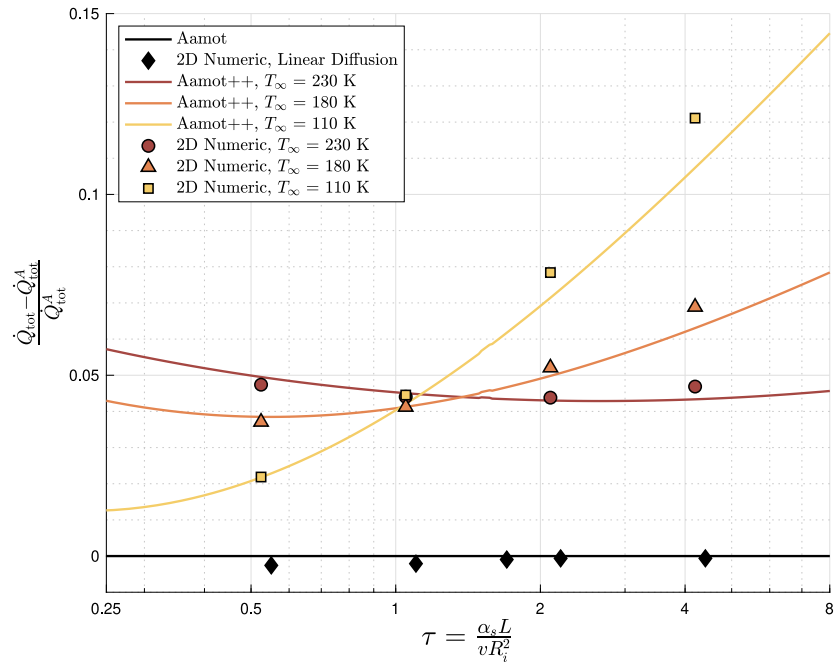
Fig. 3. The residual differences in the total heat budgets between Aamot++ and Aamot relative to Aamot is seen as a function of τ. The superscript "A" is used to denote the Aamot model. Here, it is seen that the incorporation of temperature-dependent thermal conductivity (i.e., utilizing Aamot+) has the highest impact on closing the analytic models with the numerical models as opposed to simply including every term in Eq. (2) with constant thermal conductivity.
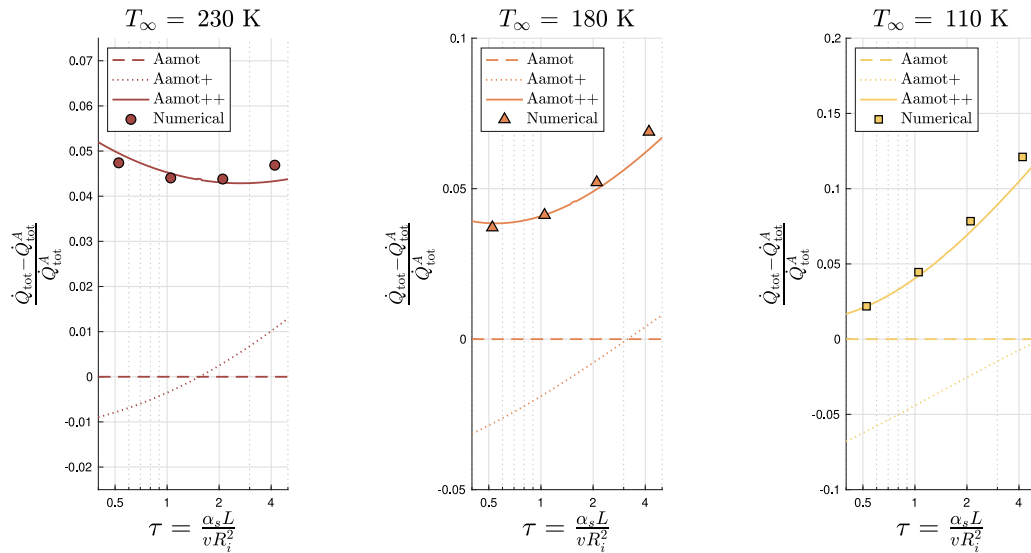

Fig. 4. Addition of nonlinear diffusion only (Aamot+) and both nonlinear diffusion and a water annulus (Aamot++) to the original Aamot model. Here, R_o is held fixed between Aamot+ and Aamot++; it can be inferred that as r^* tends lower than 1.0, disagreement between Aamot++ and Aamot+ will increase.

In the case that the ice shell segment has a uniform far-field temperature, the probe speed will be constant and the time to descend is given trivially by

$$t_d = \frac{D}{v}$$
$$= \frac{D R_i^2}{\alpha_s L} \tau(\Omega, \Theta, \epsilon) \tag{23}$$

In this case, for a given set of probe design parameters Ω and ϵ, the value of τ needs to be determined just once. Changes to the probe geometry (R_i, L) or the depth of the ice shell D affect the duration calculation in a trivial analytic way.

In the case that the ice temperature changes with depth, the descent time is determined by integrating over the varying far-field temperature. Using a coordinate system where z_d is the distance from the ice surface to the probe tip, a segment of the ice is considered from $z_d = D_1$ down to $z_d = D_2$, resulting in $D = D_2 - D_1$. The time to descend is given by

$$t_d = \int_{D_1}^{D_2} \frac{dz_d}{v}$$
$$= \int_{T_1}^{T_2} \frac{1}{v} \frac{dz_d}{dT_\infty} dT_\infty$$
$$= \frac{D R_i^2}{\alpha_s L} \bar{\tau} \tag{24}$$
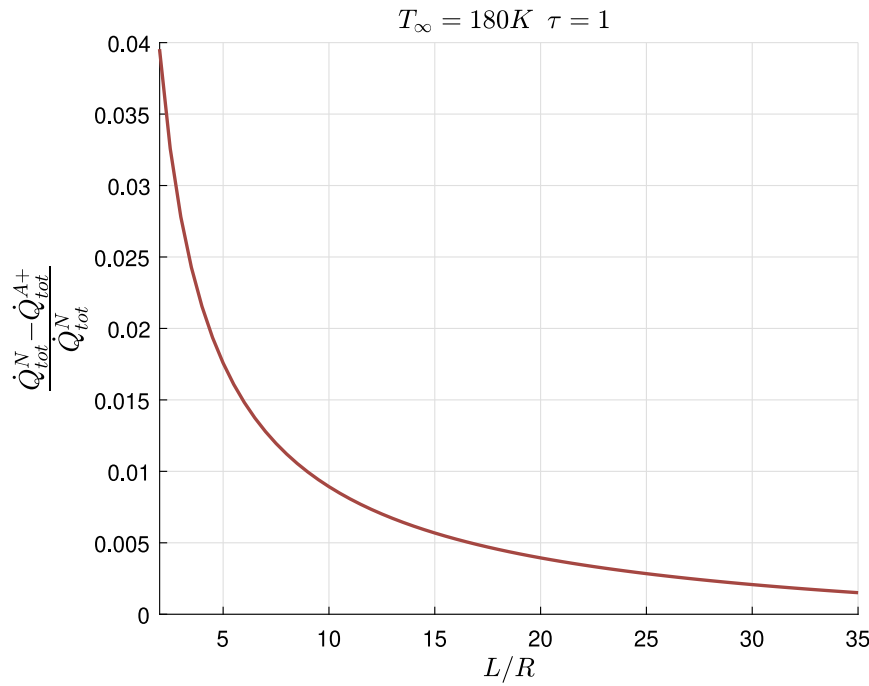
$$T_\infty = 180K \quad \tau = 1$$

Fig. 5. Aamot+ and numerical models converge on $\dot{Q}_{tot}$ as L/R tends to infinity. Here, $\tau = 1$ and $T_\infty = 180$ K. The "+" and "N" superscripts refers to the Aamot+ and numerical models respectfully.

Here the average of τ for this segment is defined to be

$$\bar{\tau} = \frac{1}{D} \int_{\Theta_1}^{\Theta_2} \tau(\Omega, \Theta, \epsilon) \frac{dz_d}{d\Theta} d\Theta \qquad (25)$$

Eq. (25) is a convolution of two terms. The function $\tau(\Omega, \Theta, \epsilon)$ is provided by the analytic probe performance models described in this paper which can be computed rapidly with high precision and can be validated empirically. The temperature gradient of the ice shell dz_d/dT_∞ may describe an unexplored region of the solar system. As such, it can have large uncertainties which must be accounted for, as is done in [8] with a Monte Carlo simulation of the Europan ice shell. The power of the analytic result for τ is that it can easily be combined with such Monte Carlo simulations. Doing so will convert a distribution of possible ice shells to a distribution of the time required to melt from the surface to the ocean of Europa, thereby quantifying the mission duration for an ice probe and its uncertainties.

The remarkable comparison between Aamot++ and the numerical models enables more accurate Monte Carlo modeling of time-to-descent. While high-fidelity numerical modeling could be employed to more precisely calculate probe heat budgets and account for non-analytic features, such as asymmetry, a rounded probe-nose, or higher-order design features, the cost of implementing these models in a Monte Carlo framework is computationally prohibitive. While realistic design features violating the relatively strict requirements of analytic models could be incorporated into numerical models, forgoing the use of the Aamot++ model, the gained accuracy within the range of τ considered is minimal. In comparison, the Aamot++ results can be effortlessly computed in ≤ 3s, whereas presented results from the numerical model require in excess of 2 CPU hours.

Future work will incorporate the Aamot++ model into a Monte Carlo framework that convolves predictions for instantaneous probe speed with models of the ice shell structure and temperature profile, similar to models described in [8]. The uncertainties in the ice shell physics are large. For example, the best estimate and $+1\sigma$ models of ice thickness in [8] differ by 100%. This far exceeds any disagreement in probe speed between the model presented here, so the Monte Carlo can treat Aamot++ as effectively exact.

4.2. Restrictions on the Aamot++ model

The Aamot++ model inherits some restrictions on its applicability; however, most of these restrictions are not prohibitive for practical probe design. One such restriction is the requirement that $L/R \gg 1$. This is a useful constraint because the total thermal cost of descending to a given depth directly scales with the cross-sectional area of the probe. Therefore, a large aspect ratio is desirable. While this restriction has yet to be exhaustively quantified, an example of convergence between analytic and numerical models is provided in Fig. 5. In the given conditions, aspect ratios less than nine initiate a greater-than-1% difference regime between numerical and analytic Aamot+ though flight-like probe designs similar to those of [6] are expected to have aspect ratios with $L/R \gtrsim 20$. In A.2, it is shown that the axial diffusion in Region B tends to become unimportant as $\tau R/L \to 0$. Conversely, end effects associated with this term will become detectable for slow moving, squat shaped probes, as might be operated in a cryogenic test bed where vertical space is limited.

Another restriction on Aamot++ is that the thickness of the water annulus must be limited so that the behavior of the flow can be captured by density-independent models. This assumption is favorable because a small gap size is a desirable design regime. Maintaining a wider annulus requires diverting more heat from descent, resulting in inefficient operation. In the 12 benchmark numerical cases with $r^* = 0.976$, the full temperature-dependence of density was considered. However, the axially-dominated flow remained unperturbed by the buoyancy force. The upper bound of validity, where the Aamot++ model for $\dot{Q}_3$ begins to diverge with the numerical model, is approximately $r^* = 0.95$. Fig. 6 shows a comparison between the numerical model, the Aamot++ model of $\dot{Q}_3$, and a more sophisticated analytic model for $\dot{Q}_3$ that uses a form of the Boussinesq approximation to allow the density of the fluid in the annulus to be dependent on temperature. This is referred to as the Temperature-Dependent Density (TDD) model. All of the 12 benchmark numerical models agree with Aamot++ to within 2% for the prediction of $\dot{Q}_3$ having high values of r^* (corresponding to a narrow annulus). As the annulus begins to widen, the models begin to diverge because the density-driven buoyancy forces captured in the numerical and TDD
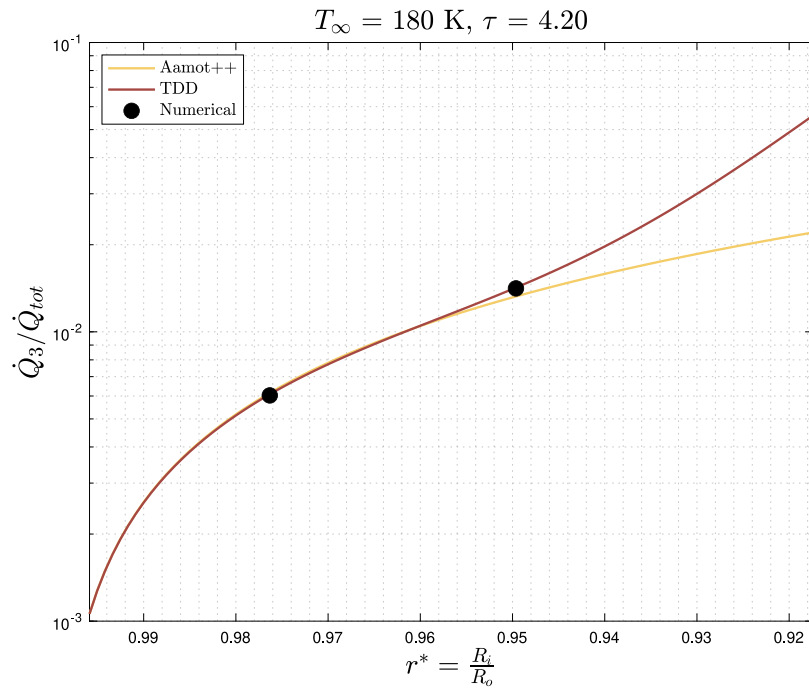
Fig. 6. The Aamot[++] model under-predicts the magnitude of $\dot{Q}_3$ compared to the numerical models and the Temperature-Dependent Density (TDD) model for smaller values of r^*, corresponding to a wider annulus.

models play a dominant role in the hydrodynamics. As a result, these models predict a larger magnitude of $\dot{Q}_3$ than Aamot[++] as r^* decreases. If the annulus grows too large, a significant portion of the supplied heat will be lost to advection, and vertical control over the probe could be compromised, though an annulus that is too narrow could result in the probe descending inefficiently, as discussed in [10,11]. Therefore, to achieve a well-constrained efficiency, proper thermal management within the hull is essential to an efficiently operated successful mission.

The class of ice probes described in this paper are cylindrical in shape. However, specific design features may deviate from this approximation, especially along the front end where thermal gradients are large. The Aamot[++] model can still be used for high-level trades and estimates of ice shell transit time (for example, see [7]), where more detailed features need developed using a complete numerical model. The numerical model described in Appendix B retains some approximations, such as a decoupling of the thermal physics and force balance, and these restrictions may need to be relaxed in order to provide a complete model

5. Conclusions

This work has shown that the Aamot model consistently underpredicts the total heat required to achieve a specific descent speed under specific environmental conditions. This results in overly-optimistic computations of descent times for probes traversing cryogenic ice, thereby weakening the validation of mission concepts to access the subsurface oceans of Europa and Enceladus. The Aamot[++] model is shown to diminish disagreements between the previous analytic model of Aamot and a full-physics numerical model. This closure in residuals is partially achieved by the addition of the water annulus, which itself provides a metric for efficient probe design. If system-level thermal management can achieve a high efficiency, then confidence can be placed in probabilistic calculations leveraging Aamot[++] to predict the time needed to reach the subsurface oceans of icy worlds.

Declaration of competing interest

The authors declare that they have no known competing financial interests or personal relationships that could have appeared to influence the work reported in this paper.

Appendix A. Notes regarding analytic equations

A.1. Derivation of Eq. (2)

Eq. (2) can be derived by starting with the heat equation for the solid phase in the reference frame where the ice is static and the probe is moving, given by

$$\tilde{\nabla} \cdot (k\tilde{\nabla}T) = \rho c \frac{\partial T}{\partial \tilde{t}} \tag{26}$$

where the tilde indicates the ice-static reference frame. This assumes that the density is unmodified by local temperature perturbations and can be treated as a constant which is an accurate approximation for a solid material under pressure. If the probe begins with its tip at $\tilde{z} = 0$ at $\tilde{t} = 0$, an arbitrary point in the ice at $\tilde{z}$ will be at a position $z = \tilde{z} - v\tilde{t}$

relative to the probe tip at a later time. Together with $\tilde{t} = t$, this defines a coordinate transformation such that

$$\frac{\partial}{\partial \tilde{t}} = \frac{\partial}{\partial t} - v \frac{\partial}{\partial z}$$
$$\frac{\partial}{\partial \tilde{z}} = \frac{\partial}{\partial z} \tag{27}$$

Further assumption of steady-state behavior in the reference frame of the probe implies that $\partial/\partial t = 0$. Substitution into Eq. (26), transformation to cylindrical coordinate, and an assumption of axial symmetry leads to Eq. (2).

A.2. Non-Dimensional Analysis of Eq. (2)

Eq. (2) is cast into a non-dimensional form with the following transformations.

$$\mathcal{U}(T) = \frac{\int_{T_\infty}^{T} c(T')\rho(T')dT'}{\int_{T_\infty}^{T_0} c(T')\rho(T')dT'}$$
$$\zeta = \frac{r}{R_o} = r^* \frac{r}{R_i}$$
$$\xi = r^{*2}\tau \frac{z}{L}$$
$$\alpha^* = \frac{\alpha(T)}{\alpha_s} \tag{28}$$

With these changes, Eq. (2) becomes

$$\left[r^{*2}\tau \frac{R_o}{L} \right]^2 \frac{\partial}{\partial \xi} \left(-\alpha^* \frac{\partial \mathcal{U}}{\partial \xi} \right) + \frac{1}{\zeta} \frac{\partial}{\partial \zeta} \left(-\alpha^* \zeta \frac{\partial \mathcal{U}}{\partial \zeta} \right) + \frac{\partial \mathcal{U}}{\partial \xi} = 0 \tag{29}$$

The boundary conditions have become $\mathcal{U} \to 0$ as $\zeta \to \infty$ and $\mathcal{U} = 1$ at $\zeta = 1$, with the inner cylinder extending from $\xi = 0$ to $\xi = r^{*2}\tau$. If the shape of the function $\alpha^*(T(\mathcal{U}))$ is specified, then the solution of Eq. (29) can depend on only the inverse non-dimensional speed scaled to the cavity radius ($r^{*2}\tau$) and the aspect ratio of the cavity (R_o/L). While the product of these parameters appears as a coefficient in the equation, only one of them appears in the specification of the boundary conditions.

The non-dimensional function $\alpha^*(\mathcal{U})$ can change for one of two reasons. The material properties can change explicitly, for example by adding impurities to the ice or simply swapping between a model of temperature-independent and temperature-dependent properties. However, even if the function $\alpha^*(T)$ is unchanged, the mapping between T and $\mathcal{U}$ can change by changing the far-field temperature T_∞. Thus, for fixed $\alpha^*(T)$, the solution to (29) will also depend on $\Theta = (T_0 - T_\infty)/T_0$. When redimensionalizing the result, the energy scale given by $\int_{T_\infty}^{T_0} c(T')\rho(T')dT'$ must be reintroduced which further introduces a dependence on Θ.

In Region B, it is reasonable to neglect the axial diffusion term (the first term in Eq. (29)), as done in the work of Aamot (and hence Aamot+ and Aamot++), provided that $\left[r^{*2}\tau R_o/L \right]^2$ is sufficiently small. As such, the approximation is best satisfied for larger aspect ratios (as seen in Fig. 5). If the large aspect ratio approximation is sufficiently met, the function f_2 depends only on the parameters $r^{*2}\tau$ and Θ with minimal loss of accuracy, as demonstrated in Figs. 3, 4, where the Aamot++ model agrees with the numerical model to within 2%.

A.3. Notes on Eqs. (4) and (13)

Eqs. (4) and (13) are derived under the assumption that the temperature contours below the probe are parallel to the melt surface so that Eq. (2) reduces to

$$0 = \frac{\partial}{\partial z} \left(-k \frac{\partial T}{\partial z} \right) + c\rho v \frac{\partial T}{\partial z}$$
$$= \frac{\partial}{\partial z} \left(\dot{q}_z'' + v \int_{T_\infty}^{T} c(T')\rho(T')dT' \right) \tag{30}$$

The result is then integrated from $z = -\infty$ to 0, and it is assumed that all the heat is absorbed by the ice so that the constant of integration is zero. This yields a uniform flux at the top of the cylinder

$$\dot{q}_z'' = -v \int_{T_\infty}^{T_0} c(T)\rho(T)dT \tag{31}$$

Integrating across a bounding disk of radius R at $z = 0$ gives

$$\dot{Q}_1 = \pi R^2 v \int_{T_\infty}^{T_0} c(T)\rho(T)dT \tag{32}$$

where the change in sign is because $\dot{Q}_1$ is defined as positive in the downward direction. For Eq. (4), the radius is taken to be $R = R_i$, and the material properties are constant. For Eq. (13), the radius is taken to be $R = R_o$, and the material properties are arbitrary functions of temperature.

A.4. Notes on Eq. (5)

For the Aamot model, the material properties are taken to be constant, and in Region B the axial conduction term is neglected. Eq. (2) then reduces to

$$\frac{1}{r} \frac{\partial}{\partial r} \left(r \frac{\partial T}{\partial r} \right) = \frac{v}{\alpha_s} \frac{\partial T}{\partial z} \tag{33}$$

The boundary conditions are given as $T = T_0$ at $r = R_i$ and $T = T_\infty$ as $r \to \infty$. The single axial derivative means that z behaves like a time coordinate with the initial condition given by $T = T_\infty$ at $z = 0$. The closed form solution is given in Section 13.5 of [13] as

$$T(r, z) = T_\infty + (T_0 - T_\infty) \frac{2}{\pi}$$
$$\times \int_0^\infty \frac{db}{b} \frac{Y_0(b)J_0(br/R_i) - J_0(b)Y_0(br/R_i)}{J_0^2(b) + Y_0^2(b)} e^{-\frac{b^2\alpha_s z}{R_i^2 v}} \tag{34}$$

where J_0 and Y_0 are the zeroth order Bessel functions of the first and second kind. Eq. (34) both solves (33) and satisfies the boundary conditions. The flux at the cylindrical surface is calculated as

$$\dot{q}_2'' = -k_s \frac{\partial T}{\partial r} \bigg|_{r=R_i}$$
$$= \frac{k_s(T_0 - T_\infty)}{R_i} \frac{2}{\pi} \int_0^\infty db \frac{Y_0(b)J_1(b) - J_0(b)Y_1(b)}{J_0^2(b) + Y_0^2(b)} e^{-\frac{b^2\alpha_s z}{R_i^2 v}}$$
$$= \frac{k_s(T_0 - T_\infty)}{R_i} \frac{4}{\pi^2} \mathcal{J}_0 \left(\frac{\alpha_s z}{R_i^2 v} \right) \tag{35}$$

where in the last line the Wronskian identity $Y_0(b)J_1(b) - J_0(b)Y_1(b) = 2/(\pi b)$ has been applied.

A.5. Derivation of Eq. (17)

A series of transient one-dimensional finite volume simulations were conducted using Ansys CFX to find the solution of Eq. (14) with a time coordinate defined as $t = z/v$. This was achieved by modeling the radial diffusion within an annular sector of the ice field surrounding the probe. The inner radius of the sector, located at $r = R_o$, was held at a constant temperature T_0, while the far-field radius was held at a constant temperature T_∞. The far-field radius was placed sufficiently far away so as to not affect the behavior close to the inner radius. For each case, the domain was initialized as $T = T_\infty$, and the heat flux at the inner radial boundary was recorded with respect to time.

The single spatial dimension enables the solution to be found rapidly. The simulations were conducted for both temperature-independent and temperature-dependent ice properties, with far-field temperatures ranging from 100 K to 270 K in 10 K increments. The results for the τ range of interest between 0.1 and 10 were found by considering the appropriate time frame in each simulation. The resulting inner boundary flux was integrated over $2\pi R_o dz$ to give the total radial heat loss $\dot{Q}_2$.
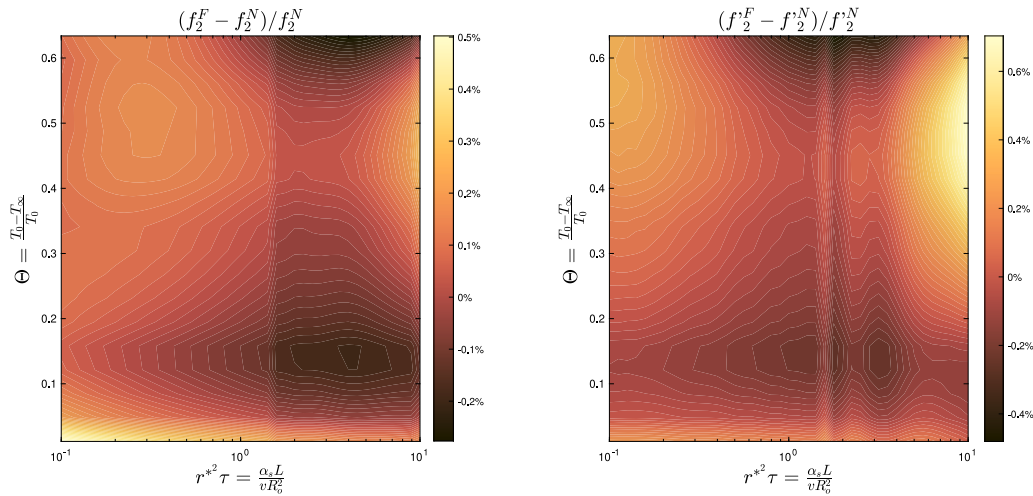
Fig. 7. Comparison of the fitted function of Eq. (17) (f_2^F) to the full numerical solution of the 1D nonlinear diffusion equation (f_2^N). Here the notation f_2' replaces $\partial_{(r^{*2}\tau)} f_2(r^{*2}\tau, \Theta)$.

For the case of temperature-independent material properties, the results were found to be in agreement with Eq. (7) of the Aamot model to within 0.2%. For the case of temperature-dependent material properties, the results were all consistent with the form of Eq. (15), demonstrating the correctness of the dimensional analysis.

Rather than providing tabulated results, a compact analytic approximation to the function f_2 was sought, defined in Eq. (15). After dividing out the leading behavior provided by the linear result, it was found that sufficient accuracy could be provided by a polynomial function that is second order in both Θ and $\ln \tau$ as described in Eq. (17). The polynomial coefficients were determined by fitting to the numerical results.

The errors between the fitted function and the numerical computation of f_2 are plotted in Fig. 7. The errors range from −0.25% to 0.5% for the region of interest, but this level of agreement should not be assumed outside the range of the fit. Additionally, the Aamot++ model utilizes the derivative of f_2 in Eq. (19) to model the flux at the rear end of the probe. The analytic derivative of the fitted result was compared to the numerical computation, and those results are also shown in Fig. 7.

It is noted that the polynomial function of Eq. (17) has no quadratic cross term proportional to $\Theta \ln \tau$. Including this term added a coefficient that was close to zero, and the quality of the fit was not noticeably improved. This suggests that some simplifying mechanism may be at work, leading to a result that is the product of separate functions over Θ and τ. While interesting, this feature is not investigated further in this paper.

A.6. Notes on Eq. (19)

In deriving Eq. (19) from (18), an important step is evaluating the radial flux at $r = R_o, z = L$. This can be related to the total heat $\dot{Q}_2$ trivially by

$$\dot{q}_2'' \big|_{z=L} = \frac{1}{2\pi R_o} \frac{\partial \dot{Q}_2}{\partial L} \tag{36}$$

Furthermore, note that the only L dependence in Eq. (15) is given by the argument of f_2, so that

$$\frac{\partial f_2}{\partial L} = \frac{\alpha_s}{R_o^2 v} \partial_{(r^{*2}\tau)} f_2 \tag{37}$$

and so

$$\dot{q}_2'' \big|_{z=L} = \frac{k_s (T_0 - T_\infty)}{2 R_o} \partial_{(r^{*2}\tau)} f_2 \tag{38}$$

Appendix B. Numerical methodology

A finite volume model of a descending ice probe was developed using the meshing utility Ansys ICEM CFD and the CFD solver Ansys CFX (Ansys Inc., Canonsburg PA, USA). The model was formulated to simulate the hydrodynamics and heat transfer of an axisymmetric descending ice probe without most of the Aamot-class model restrictions. Features such as fillets and hull-tapering were included in the model to encourage the calculated phase interface to form vertically, allowing for direct comparison with Aamot++ at the location $r = R_o$.

While such a high-fidelity model is ideal for design evaluation, its computational cost is prohibitive when used in high-level parametric studies. Therefore, a second class of numerical models (a somewhat more restrictive version of the original numerical model) was developed for use in the comparison in Section 3. To distinguish the numerical models, the least restrictive model is referred to as the "fully-coupled" model while the simplified version is referred to as the "segregated mode". As the names suggest, the fully-coupled model resolves both the ice and water domain simultaneously and hence requires no *a priori* assumptions or requirements for the phase boundary location, which as a result, is an output of the model. Conversely, the phase boundary in the segregated model is given as an input rather than an output, allowing for both domains to be solved separately. In turn, the required heat flux $\dot{q}''$ on the probe wall to maintain the imposed phase-boundary location is an output to the model. This requires an iterative approach in the liquid region to ensure thermal compatibility between the domains at the phase boundary. It will be shown that for a representative case, the segregated model solution closely matches that of the fully-coupled solution.

B.1. Fully-coupled approach

The fully-coupled model is governed by the following system of equations:

$$\nabla \cdot (\rho \vec{v}) = 0 \tag{39}$$

$$\nabla \cdot (\rho \vec{v} \vec{v}) = -\nabla p + \nabla \cdot \sigma + (1 - f_L) C(v - \vec{v}) + f_L \vec{g}(\rho - \rho_{ref}) \tag{40}$$

$$\nabla \cdot (\rho \vec{v} h) = \nabla \cdot (k \nabla T) \tag{41}$$

Here, σ is the viscous stress tensor for a Newtonian fluid, C is an arbitrarily large constant of units kg/(m³ s), $\vec{g}$ is the local gravity vector, ρ_{ref} is the maximum liquid density, and h is the local enthalpy used to calculate f_L - the local mass fraction of the liquid phase. The reference enthalpy values $h = -H$ and $h = 0$ correspond to solid and liquid water at $T = T_0$ respectively. All material properties are assumed
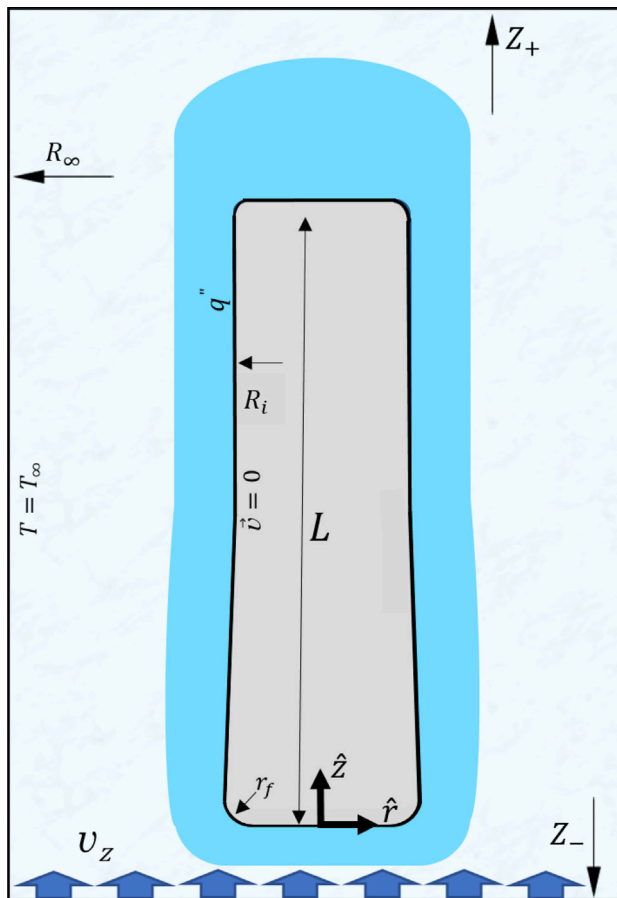
Fig. 8. Domain and boundary conditions for the fully-coupled model.

Table 3
Values for boundary geometries in the dimensionful numerical models.

Dimension	L	L'	R_∞	R_o	R_{i+}	R_i	r_f	Z_+	Z_-	δ_r	δ_z
Value [m]	2.09	1.2	1.85	0.1211	0.12101	0.1182	0.01	30	−1	2.8e−3	0.9e−4

Table 4
Difference in interfacial location, advective quantities, heat budget in the water annulus between the segregated (S) and fully-coupled (FC) models for $T_\infty = 110$ K and $\tau = 0.5$. It should be noted that temperature RMSE and normalization procedure was conducted in units of Celsius.

$T_\infty = 110$ K, $\tau = 0.5$					
	Gap size		Fluidics variables @ $z = L$		
	δ_z	δ_r	$v_z(r)$	$T(r)$	
$\frac{\mathrm{RMSE_{FC:S}}}{\max_{FC}} \times 100\%$	4.985e−4	2.490e−2	1.5854	0.6582	
	Heats				
	$\dot{Q}_{\mathrm{tot}}$	$\dot{Q}_0$	$\dot{Q}_1$	$\dot{Q}_2$	$\dot{Q}_3$
$\frac{\dot{Q}_{i,S} - \dot{Q}_{i,FC}}{\dot{Q}_{i,FC}} \times 100\%$	0.337	−0.4731	1.3589	0.2219	2.6009

known functions of temperature only. The boundary conditions for the model are illustrated in Fig. 8, and dimensions are given in Table 3. To close the momentum equation, the reference pressure is set to a constant at the trailing far-field.

The source term in the momentum equation, $(1 - f_L)C(v - \vec{v})$, is used to impose the reference frame motion in the ice. This requires a fine mesh grid (in the phase interface neighborhood) and proportionately small pseudo time step to solve, thereby increasing the CPU demands to prohibitive levels. Therefore, the segregated model formulation,
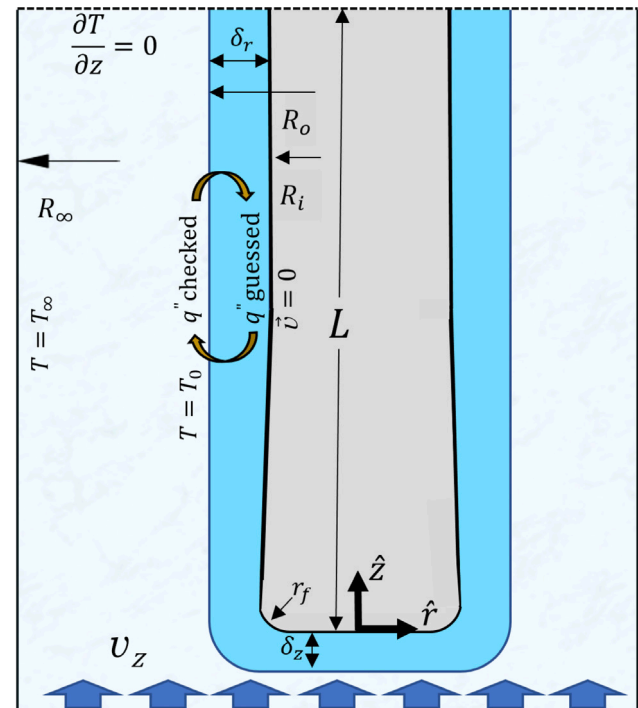

Fig. 9. Domain and boundary conditions for the segregated model.

consisting of separate ice and water domains, was adopted to produce the benchmark cases discussed throughout this work.

B.2. Segregated approach

For the solid domain, the governing equation is

$$\rho c \nabla T = \nabla \cdot (k \nabla T) \tag{42}$$

For the liquid domain, the system of equations is

$$\nabla \cdot (\rho \vec{v}) = 0 \tag{43}$$

$$\nabla \cdot (\rho \vec{v} \vec{v}) = -\nabla p + \nabla \cdot \sigma + \vec{g}(\rho - \rho_{ref}) \tag{44}$$

$$\nabla \cdot (\rho \vec{v} h) = \nabla \cdot (k \nabla T) \tag{45}$$

Both domains are subject to the boundary conditions given in Fig. 9. The ice domain is trivially solved first as all boundary conditions are known a priori for a given phase boundary location. In the liquid domain, while the boundary conditions on the phase boundary are known, it is not known what thermal conditions on the hull will satisfy the geometric and thermal constraints on the water annulus. Therefore, an iterative approach is required to determine $\dot{q}''$ on the probe wall that yields a compatible heat flux distribution on the imposed phase boundary. This is evaluated by matching the heat flux from both model domains at the interface. Over the last 50% of the probe's length, the average RMS heat flux error at the boundary across all test cases was 0.19%.

To compare the fully-coupled and segregated models, the segregated solution for the probe wall heat flux $\dot{q}''$ to the benchmark case $\tau = 0.5$ and $T_\infty = 110$ K was imposed as $\dot{q}''$ in the fully-coupled model (as shown in Fig. 8) with the probe top above $z = L$ assumed adiabatic. The fully-coupled model was then solved for $\tau = 0.5$ and $T_\infty = 110$ K. If imposing the vertical phase-boundary a priori does indeed impact the solution $\dot{q}''$, and the segregated approach has sufficiently iterated for $\dot{q}''$, then the phase boundary location computed by the fully-coupled model should match the location $r = R_o$ imposed in the segregated model.

B.3. Fully-coupled versus segregated comparison

Table 4 contains metrics comparing solutions obtained with the fully-coupled and segregated methods for a benchmark case. The quantities first considered are the root mean square errors (RMSE) of both the r and z interface locations, normalized by the maximum δ_r and δ_z values in the fully-coupled solution. Next, the z-component of $\vec{v}$ ($v_z(r)$) and the water temperature ($T(r)$) in the annulus at the location $z = L$ are compared between the two solution methods. This comparison assesses the impact of truncating the domain at $z = L$. Finally, each of the heat terms $\dot{Q}_0$ through $\dot{Q}_3$ are compared. Discrepancies in part can be attributed to the slight spatial inconsistency of boundary locations; however, the disagreement in heat budget between the two methods is less than half a percent, well within the disagreement between the 12 benchmark cases solved with the segregated method and Aamot++ heat budgets.

References

[1] P. do Vale Pereira, et al., Experimental results of melt probes in cryogenic ice for a future europa lander, 2020, http://dx.doi.org/10.1002/essoar.10505346.1.

[2] B. Sherwood, Strategic map for exploring the ocean-world enceladus, Acta Astronaut. 126 (2016) 52–58, http://dx.doi.org/10.1016/j.actaastro.2016.04.013.

[3] K. Konstantinidis, et al., A lander mission to probe subglacial water on saturn's moon enceladus for life, Acta Astronaut. 106 (2015) 63–89, http://dx.doi.org/10.1016/j.actaastro.2014.09.012.

[4] B. Sherwood, et al., Exploring the ocean worlds, in: 2018-OCEANS - MTS/IEEE Kobe Techno-Oceans (OTO), 2018, pp. 1–10., http://dx.doi.org/10.1109/OCEANSKOBE.2018.8559155.

[5] S. Howell, et al., Ocean worlds exploration and the search for life, 2020, https://arxiv.org/abs/2006.15803.

[6] W. Zimmerman, et al., Cryobot: An ice penetrating robotic vehicle for mars and europa, J. Molecular Catalysis A-Chemical - J MOL CATAL A-CHEM (2001) 1/311 – 1/323 vol. 1, http://dx.doi.org/10.1109/AERO.2001.931722.

[7] D. Woerner, Radioisotope heat sources and power sources for enabling ocean worlds subsurface and ocean access missions, Bull. AAS (2020) URL: https://baas.aas.org/pub/2021n4i322.

[8] S. Howell, The likely thickness of europa's icy shell, Planet. Sci. J. 2 (129) (2021).

[9] H.W.C. Aamot, Heat Transfer and Performance Analysis of a Thermal Probe for Glaciers, Technical Report 194, Cold Regions Research and Engineering Laboratory, Hanover New Hampshire, 1967.

[10] S. Ulamec, et al., Access to glacial and subglacial environments in the solar system by melting probe technology, Environ Sci Bio/Technol 6 (2007) 71–94, http://dx.doi.org/10.1007/978-1-4020-6285-8_1.

[11] B. Cassler, et al., Constraints on the behavior of a descending ice probe due to force balance, Acta Astronaut. 189 (2021) 606–614.

[12] K. Schüller, J. Kowalski, Melting probe technology for subsurface exploration of extraterrestrial ice - critical refreezing length and the role of gravity, Icarus 317 (2018) http://dx.doi.org/10.1016/j.icarus.2018.05.022.

[13] H. Carslaw, J. Jaeger, Conduction of Heat in Solids, in: Oxford Science Publications, Clarendon Press, 1986, URL: https://books.google.com/books?id=y20sAAAAYAAJ.

[14] J. Pátek, J. Hrubý, J. Klomfar, M. Součková, A. Harvey, Reference correlations for thermophysical properties of liquid water at 0.1 MPa, J. Phys. Chem. Ref. Data 38 (1) (2009) 21–29, http://dx.doi.org/10.1063/1.3043575.

[15] D. Friend, R.B. Dooley, Revised Release on the Equation of State 2006 for H2O Ice Ih, Technical Report, International Association for the Properties of Water and Steam, 2009.

[16] O. Andersson, A. Inaba, Thermal conductivity of crystalline and amorphous ices and its implications on amorphization and glassy water, Phys. Chem. Chem. Phys. 7 (2005) 1441–1449, http://dx.doi.org/10.1039/b500373c.

[17] R. Shah, A. London, Laminar Flow Forced Convection in Ducts: A Source Book for Compact Heat Exchanger Analytical Data, Elsevier Science, 2014, URL: https://books.google.com/books?id=D-JbAwAAQBAJ.

[18] W.R.C. Phillips, P.J. Mahon, On approximations to a class of jaeger integrals, Proc.: Math. Phys. Eng. Sci. 467 (2136) (2011) 3570–3589, URL: http://www.jstor.org/stable/23058750.

[19] F. Crameri, Scientific colour maps (version 7.0.0), Zenodo (2021) http://dx.doi.org/10.5281/zenodo.4491293.